COASTAL PROTECTION

Mechanisms and frequency-size statistics of failures characterizing a coastal cliff partially protected from the wave erosive action

Giuseppe Esposito[1] · Fabio Matano[2] · Marco Sacchi[2] · Riccardo Salvini[3]

Abstract

Landslides and surface erosion are major processes controlling the progressive recession of many rocky cliffs along the Italian coastline. Nevertheless, many coastal settlements were built along cliffed sectors prone to rapid collapses. This represents a serious risk for tourists and living people, as well as for buildings, roads and railway networks. The densely urbanized coastline of the Campi Flegrei active volcanic district is one of the rocky coastal areas of South Italy mostly exposed to the recession. Here, coastal cliffs are made by volcaniclastic deposits and include remnants of ancient volcanic edifices formed in the last 15 ka. Due to petrographic, geotechnical and geostructural properties of volcaniclastic deposits, these cliffs have been affected by rapid recession since their origin. This research focuses on a cliff of the Campi Flegrei coastaline (Torrefumo, Monte di Procida) which, although currently protected from the sea waves by a seawall, is still retreating. We assessed the ongoing recession using a change detection analysis, based on accurate topographic data acquired with two terrestrial laser scanning surveys executed in 2013 and 2016. The quantitative comparison of 3D point clouds datasets allowed detecting 191 cliff failures. We verified that the frequency-magnitude distribution of the detached blocks followed an inverse power law, and most of the involved volumes were between 0.01 and 1 m^3. Retreat rates of different cliff sectors varied from 0.001 to 0.025 m/year. Our analysis also allowed us to recognize slope failure mechanisms and distinguish rock falls from grain-by-grain surficial erosion.

Keywords Terrestrial laser scanning · Change detection · Coastal cliff · Rock fall · Erosion · Frequency-volume distribution

✉ Giuseppe Esposito
giuseppe.esposito@irpi.cnr.it

1 Research Institute for Geo-Hydrological Protection of the Italian National Research Council (CNR-IRPI), Via Cavour 4/6, 87036 Rende, CS, Italy

2 Research Institute of Marine Sciences of the Italian National Research Council (CNR-ISMAR), Calata Porta di Massa, Porto di Napoli, 80133 Naples, Italy

3 Department of Environment, Earth and Physical Sciences, Centre of GeoTechnologies, University of Siena, Via Vetri Vecchi 34, 52027 San Giovanni Valdarno, AR, Italy

1 Introduction

Terrestrial laser scanning (TLS) is one of the most used techniques to perform geomorphic analysis in coastal environments. TLS-based studies of sea cliffs, for example, range from the geostructural analysis (Martino and Mazzanti 2014; Matano et al. 2015, 2016; Somma et al. 2015) to the evaluation of erosion processes and hazard assessment (Rosser et al. 2005; Collins and Sitar 2008; Lim et al. 2011; Katz and Mushkin 2013; Kuhn and Prüfer 2014; Dewez et al. 2013). Often, the occurrence of limited space at the cliff toe or sea waves breaking directly on the cliff face may hamper ground-based topographic surveying, or limit their applicability. Particularly, rocky cliffs characterized by steep and rough morphologies are likely to subject to possible shadowing and/or occlusion effects, eventually resulting in an incomplete sampling of the surface (Passalacqua et al. 2015). Terrestrial laser scanners can be also used as permanent monitoring systems for detecting cliff topographic

changes in near real-time (Rosser et al. 2017; Williams et al. 2018).

Many catalogues of cliff failures worldwide were compiled on the basis of multitemporal TLS surveys (e.g., Rohmer and Dewez 2015; Katz and Mushkin 2013; Collins and Sitar 2008). TLS allows detecting very small levels of signals even in a noisy dataset (Kromer et al. 2017). This is particularly important for identifying small-scale failures occurring along coastal cliffs that, in some cases, can be precursors of major collapses (Rosser et al. 2007). Inventory data are generally employed to evaluate frequency-magnitude (volume or area) distributions (e.g., Dong and Guzzetti 2005; Marques 2008; Young et al. 2011) and spatial–temporal relationships of cliff instability (Rosser et al. 2007). Understanding the spatial distribution of cliff failures may be of great interest in obtaining information on external processes and environmental conditions that predispose or initiate sea-cliff instability (Rohmer and Dewez 2015).

As recognized in several geological settings, the cumulative frequency of mass wasting areas or volumes is approximated by a power law scaling (Pelletier et al. 1997; Hungr et al. 1999; Santana et al. 2012). Specifically, the empirical distributions of landslide volumes described in the literature obey almost invariably a negative power law that may vary according to landslide types, local morphology and lithological conditions, as well as on the methods of data acquisition and the different approaches to estimate the failures distribution (Brunetti et al. 2009). The high level of detail characterizing the TLS systems prevents an undersampling of failures in the smaller volume ranges that, in frequency-magnitude distributions obtained with traditional techniques, is often responsible of a rollover effect (Tebbens 2020 and references therein). The predictive effectiveness of power law-based models depends on the identification of constraints controlling the scaling exponents, as well as on the spatial and temporal resolution, quality and completeness of the used datasets (Stark and Guzzetti 2009; Brunetti et al. 2009). According to Gilham et al (2018), the frequency of failure events along coastal cliffs is generally much higher than that of terrestrial cliffs, which makes the former ideal for magnitude-frequency analysis. This type of statistics represents a fundamental tool for the prediction of future cliff instabilities and retreat scenarios, and for a quantitative risk assessment (Barlow et al. 2012; Gilham et al. 2018).

Even if advanced geomatic techniques have greatly improved accurate measurements of cliff erosion, the understanding of the mechanisms of coastal cliff retreat and relationships with environmental conditions remains difficult. According to Letortu et al. (2015), retreat occurs in "jerks", generated by the interaction of both internal factors (e.g., rock strength and structure) and external factors (e.g., rainfall, temperature variations, and wave action), so that an effective monitoring of retreat processes requires long-term topographic measurements on a high spatial and temporal resolution. TLS datasets provide therefore a significant contribution to the debate on the dominance of marine versus subaerial forcing in controlling the cliff erosion dynamics.

This work discusses the results of a TLS-based analysis of a coastal cliff located in the densely urbanized volcanic area of Campi Flegrei, in southern Italy. The cliff toe is actually not in direct contact with the seawater because of a seawall realized in the 80′s to contrast the wave erosive action. We have selected this type of cliff to analyze the erosional dynamics in case of a limited influence of marine processes. Consequently, we performed two repeated TLS surveys (in 2013 and 2016) and compared the acquired 3D point clouds using a "multiscale model to model cloud comparison" (M3C2) technique (Lague et al. 2013). This change detection method has been successfully applied by many Authors in different landscapes, including coastal settings (Barnhart and Crosby 2013; Dewez et al. 2016; Esposito et al. 2017a, b; Westoby et al. 2016; Caputo et al. 2018; Darmawan et al. 2018). Results of the change detection were used to develop an inventory of slope failures, and characterize both the frequency-volume distribution and mechanisms controlling the cliff recession. In general, this study gives a contribution to the scientific literature dealing with the TLS-based analysis of cliff erosion, highlighting the high potential of TLS in developing accurate frequency-magnitude distributions of failures, and provides new insights about geomorphic processes controlling the recession of cliffs made of pyroclastic deposits. In addition, volume measurements may inform modeling parameters aimed at quantitative risk assessment, and validation of model outputs.

2 Geological setting

The research was conducted on the Torrefumo cliff, located in the municipality of Monte di Procida, along the coastline of the Campi Flegrei volcanic area, Italy (Fig. 1). The cliff is ca. 1320 m long and has an elevation between 25 and 110 m above sea level (a.s.l.). The slope angles reach up to 90° towards the top of the cliff. The base of the cliff is protected by a continuous seawall (Fig. 1) characterized by an average height of 4 m a.s.l., that impedes a permanent inundation. The space between the seawall and the cliff toe is occupied by marine sand, anthropogenic deposits and a talus of debris derived from the cliff erosion, as well as by a small, wave-pond lake (Fig. 1).

According to Perrotta et al. (2011), the oldest rocks of the Campi Flegrei caldera (i.e. > 74 ka BP) crop out along the coastal cliffs that board the Monte di Procida promontory. These volcaniclastic deposits derive from the activity of three different monogenic volcanoes, San Martino, Vitafumo, and Miliscola, and belong to the Vivara
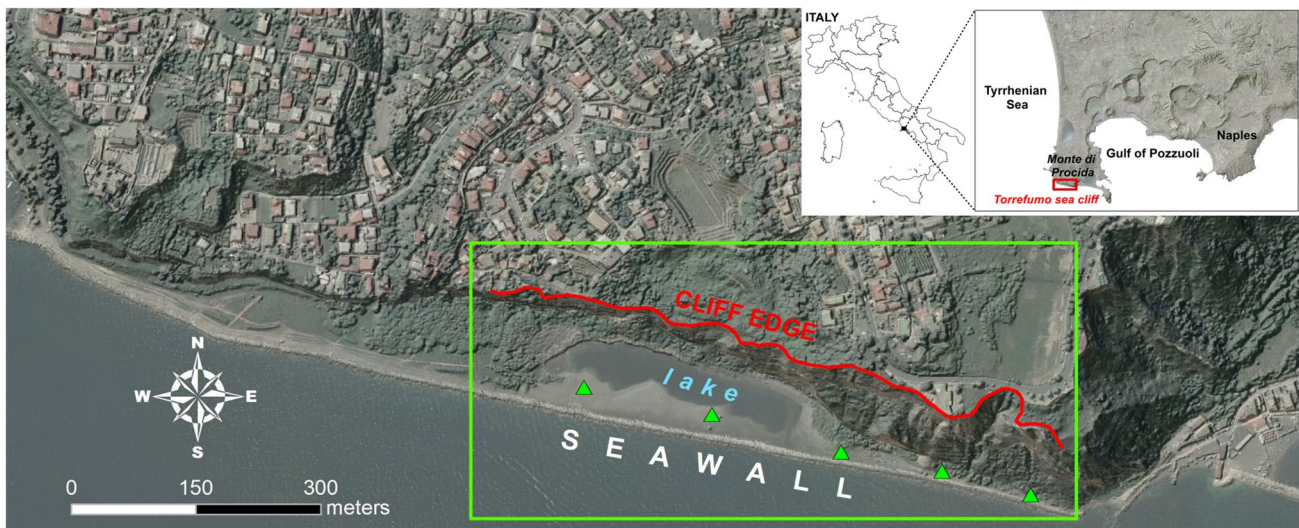
Fig. 1 Aerial image of the Torrefumo study site modified from Esposito et al. (2018). The inset map shows the location of the Campi Flegrei volcanic district, and the rectangles highlight location of the analyzed cliff. The triangles indicate the position of scan stations

Formation (Fig. 2). The products of the Vitafumo and Miliscola tuff cones form part of the Torrefumo cliff face. The lower part of the Vitafumo succession consists of layered yellow tuffs, whereas the upper is represented by reddish coarse pyroclastic rocks laterally passing to coarse surge beds with reddish pumices (Rosi and Sbrana 1987). The Miliscola succession is made up by valley-ponding, poorly sorted deposits formed by the alternation of ash and pumice layers, passing upwards to plane-parallel pumice lapilli and minor cross-stratified ash beds. These deposits mantle the underlying edifice of the Vitafumo tuff cone and become thicker towards its eastern flank (Perrotta et al. 2011). The Miliscola succession is in turn overlain by pumice and ash beds of the Serra Formation (> 39 ka BP) (Fig. 2), which is represented by fall deposits and pyroclastic flows originating from a series of consecutive eruptions. The Campanian Ignimbrite deposits (ca. 39 ka BP) separate the products of pre-caldera and post-caldera activity. In the Monte di Procida area, theses deposits are mostly represented by coarse, lithic-breccia with welded horizons that are included in the Breccia Museo Formation (Rosi and Sbrana 1987; Rosi et al. 1996; Orsi et al. 1996; Perrotta et al. 2006). The oldest unit of the post-caldera succession is represented by the Solchiaro Formation (Fig. 2) which is formed, from bottom to top by (i) dark gray scoria with intercalated gray ashes, ascribable to the Torregaveta volcano whose remnants were recognized in the northwestern side of Monte di Procida hill, and (ii) partially lithified to non-lithified grey tuffs, originated from the Solchiaro Tuff Ring, the youngest vent of Procida Island (Perrotta et al. 2011). Up in the sequence follow coarse and fine layers, and lenses of yellow pyroclastic deposits of the Neapolitan Yellow Tuff Formation (Fig. 2)

(Scarpati et al. 1993). The succession terminates with the Torre Cappella tephra that consists of a stratified succession of incoherent ash and pumice lapilli beds, and two ash layers (< 5 ka BP) separated by paleosols.

As pointed out by Esposito et al. (2018), quantitative studies on the erodibility of these cliff-forming lithologies are lacking. However, as general behavior, the erosional response seems to progressively increase from welded tuff or ignimbrite to partly consolidated or loose pumiceous and ash deposits, according to textural, mineralogical and weld-bonding properties.

3 Methods

3.1 Terrestrial laser scanning

In this study, a Riegl™ VZ-1000 terrestrial laser scanner was employed. This scanner is based on the time-of-flight technology and is classified as a long-range instrument due to a reflectorless maximum range of 1,400 m. The effective measurement rate can reach 122,000 pts/s at a frequency of 300 kHz. Measurement precision is nearly 5 mm at one sigma (68%), at 100 m range under Riegl test conditions, with a laser spot size of 7 mm.

TLS data related to the 700 m long analyzed sector of the Torrefumo cliff were acquired during May 2013 and January 2016 from 5 scan stations positioned along the cliff toe (Fig. 1). For each survey, 5 partially overlapped 3D point clouds were collected at a distance of 30÷100 m from the cliff face, with an average point spacing of 0.03 m.

Fig. 2 Cliff geological profile modified from Esposito et al. (2018). The rectangle highlights the cliff section shown in the photograph. Note the numerous buildings located at the cliff top
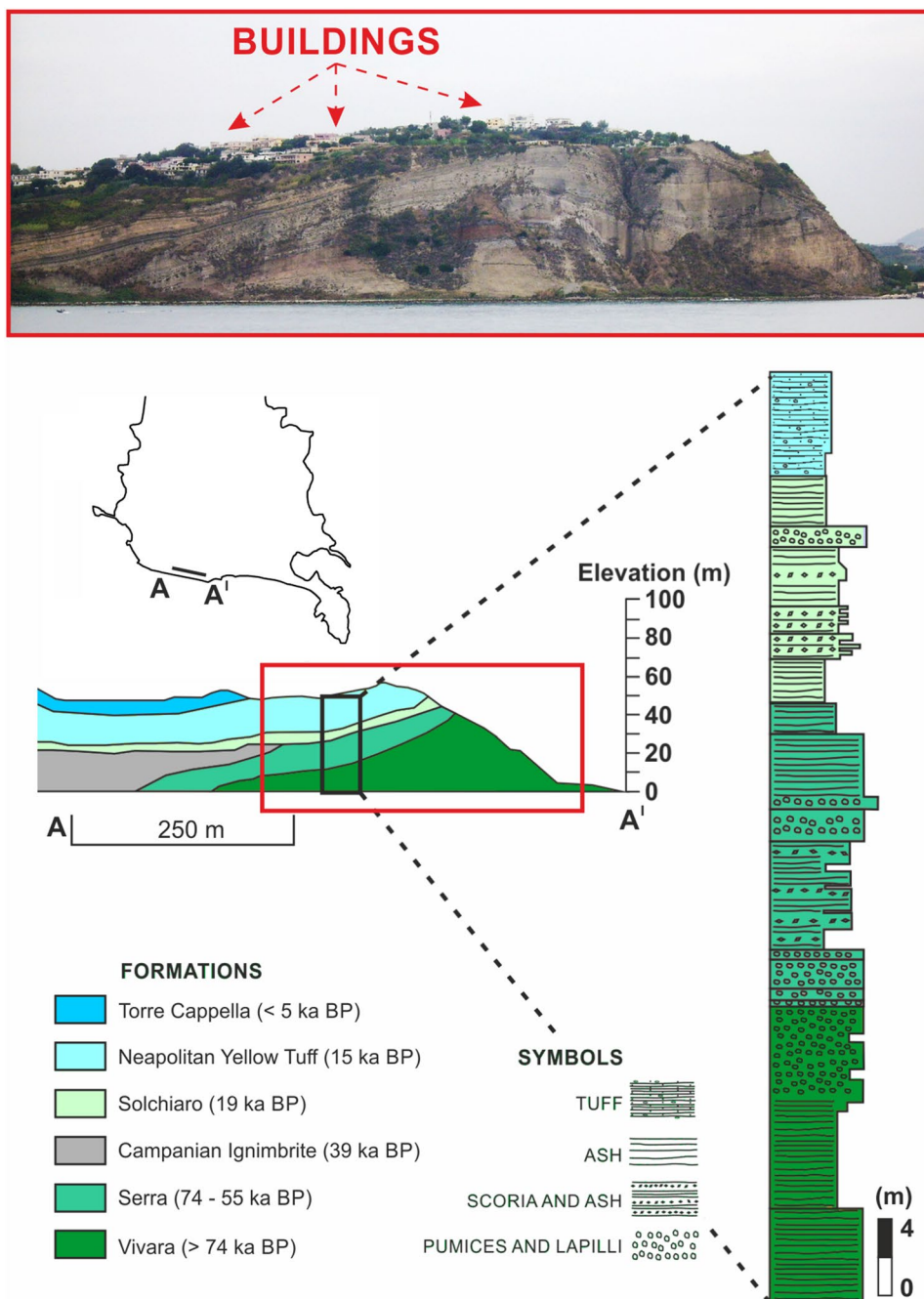
Generally, by georeferencing the point clouds or combining them from multiple scans into a single point cloud, registration errors are introduced. In change detection analyses, these inevitably increase the uncertainty and unreliability of derived changes. Taking into account this issue, the acquired data were not georeferenced by means of topographic targets, benchmarks, reflectors or other types of ground control points (GCPs), so that the corresponding 3D point clouds of different epochs could be compared independently, without combining them into single point clouds. This was also constrained by the steep morphology of the cliff site and

its inaccessibility for the positioning of GCPs. Before the comparison stage (i.e. change detection), the raw point clouds were manually filtered to exclude erroneous points (i.e. vegetation and/or points outside the area of interest) by using the CloudCompare software (www.cloudcompa re.org). Afterwards, the corresponding multitemporal point clouds were aligned in pairs, using the iterative closest point (ICP) best-fit algorithm (Besl and McKay 1992) implemented in the Trimble™ RealWorks software (Fig. 3). The ICP best-fit alignment is a fast and reliable approach that avoids the time-consuming installation of targets over wide,
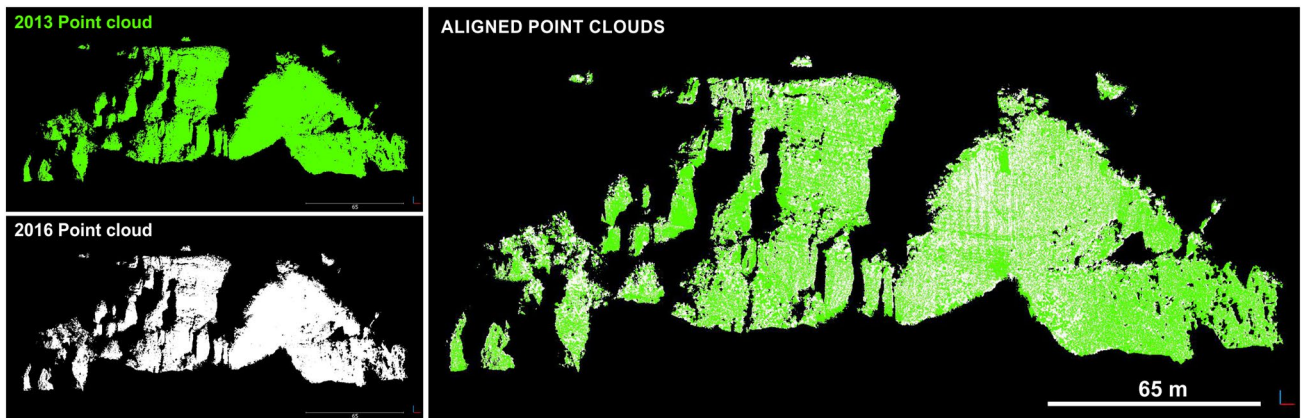
Fig. 3 Visual example of a successful alignment performed between two multitemporal 3D point clouds referred to the same area

morphologically articulated or steep slopes, and reduces the uncertainty due to the identification of the exact location of targets on point clouds characterized by variable densities (Fey and Wichmann 2017). In the ICP algorithm, a point cloud, referred as reference cloud, is kept fixed whereas the other one (moving point cloud) is moved to best match the reference. The algorithm iteratively revises the transformation (combination of translation and rotation) needed to minimize the distance from the moving to the reference point cloud. It is worth noting that, as pointed out by Kromer et al. (2015), an accurate alignment requires high and consistent point density (low point spacing).

3.2 Change detection analysis

The change detection analysis we present here aims at deriving geomorphic changes corresponding to 3D topographic distances between the acquired multitemporal point clouds, calculated along slope-dependent normal vectors.

To calculate such distances, we used the M3C2 plug-in of CloudCompare, implemented by Lague et al. (2013). As M3C2 parameters, extensively described in Esposito et al. (2017a, b), we adopted those estimated automatically by the plug-in, except the co-registration errors between the comparing point clouds (i.e. level of detection—LOD). To evaluate these errors, we followed the empirical approach developed by Collins et al. (2012). According to these authors, from each of the five pairs of aligned point clouds, we extracted 7 or 8 patches of points corresponding to rock outcrops of 3×3 m considered as "stable" during the investigated time interval (e.g., Fig. 4). Evaluation of the stability of the patched cliff portions was based on: (i) a visual inspection of the outcrops in the field, (ii) detailed photographs acquired during the surveys, (iii) statistics of distances between the corresponding patch-related points of the two epochs computed by using the Cloud-to-Cloud tool (C2C) of CloudCompare. This tool was chosen because it allows calculating the nearest neighbor distance between
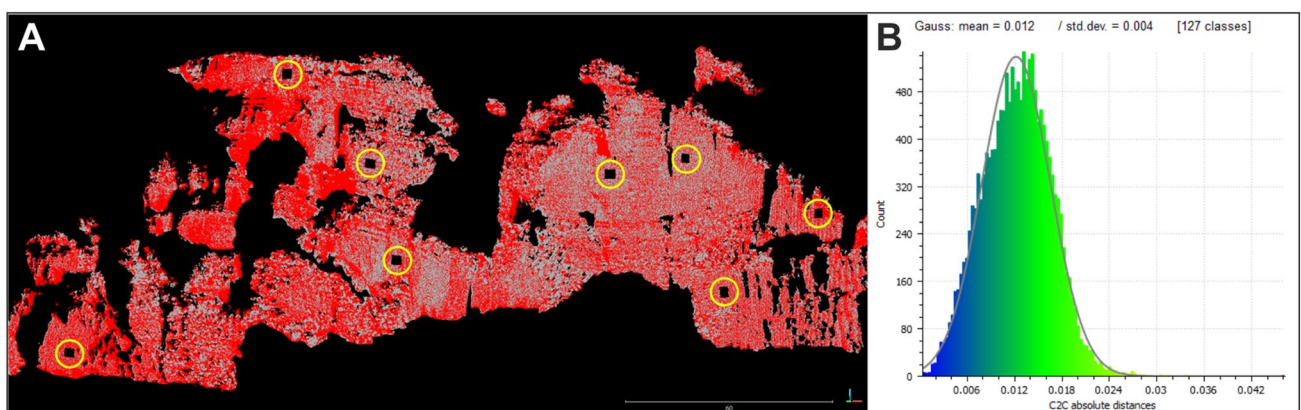

Fig. 4 **a** The circles highlight the location of point cloud patches related to "stable" zones of the cliff. **b** Example of normal distribution of distances calculated between two multitemporal patch-related clouds

342

Rendiconti Lincei. Scienze Fisiche e Naturali (2020) 31:337–351

two "reference" and "compared" cloud datasets in a bi-dimensional space, and it does not require any preliminary specification of the error. The stability of the selected rock outcrops was thus confirmed if the calculated patch-related distances were normally distributed like in Fig. 4, with values of the mean (μ) and standard deviation (σ) in the order of few centimeters or millimeters. As a final step, for each of the five change detection analyses, the average of the 7/8 patch-related distances, determined at two standard deviations ($\mu + 2\sigma$), was calculated and adopted as co-registration error. In this way, the calculated empirical errors were compared with those given by RealWorks software after the ICP-based point clouds alignment, to evaluate their accordance and obtain an indirect validation of the applied procedure.

3.3 Calculation of failures magnitude and statistical analysis

By means of the M3C2 plug-in of CloudCompare, cliff zones characterized by significant changes (i.e. distances greater than the level of uncertainty estimated by the plug-in), were identified. Since these zones corresponded to those affected by cliff failures in the 2013–2016 considered time span, both the related scar areas and volumes were calculated in CloudCompare with the following stepwise process. After the identification phase, both the compared clouds were manually clipped accordingly. The clipped cloud patches were then merged, obtaining the 3D point clouds of the detached rock blocks (Fig. 5). The latter were meshed using the Poisson Surface Reconstruction plug-in (Kazhdan et al. 2006) included in CloudCompare. After the meshing

operation, the suitable fitting of meshes with the original point clouds was verified visually, in a way to avoid overestimation or underestimation of volumes. Finally, the mesh volume and 2D area of the scar were calculated for each collapsed rock block.

The relationship between the cumulative frequency and volume of all failures detected along the entire analyzed cliff sector was approximated with a simple power law function, using a log binning procedure to define the volume classes. To take into account the issue that small magnitude failures may determine in power law fitting (i.e. "rollover" effect described by Malamud et al. 2004), a further frequency-volume curve, fitting only volumes greater than 0.03 m^3, was estimated. The two curves were then compared, evaluating the related goodness-of-fit by means of R^2. The statistical relationships between scar area, thickness and volume of the identified detached blocks were also evaluated.

To characterize the spatial distribution of detected failures along the surveyed cliff, also with respect to geological formations highlighted in Fig. 2, point clouds of both the cliff (2013) and failures were loaded in ESRI™ ArcGis software, according to an YZ projection plane (i.e. frontal view of the cliff face). Here, the cliff-related point clouds were interpolated with the "Las to raster" tool using a cell size of 20 cm. Taking as reference 16 rectangles characterized by a short side of 50 m (Fig. 6), the obtained model was then subdivided into 16 individual raster layers, corresponding to likewise cliff sectors. Each raster was analyzed in ArcGis to calculate the related 2D- and 3D-area. In addition, the total volume of detached blocks, the total area of scars, and the potentially unstable volume were calculated for each sector. The total areas and volumes
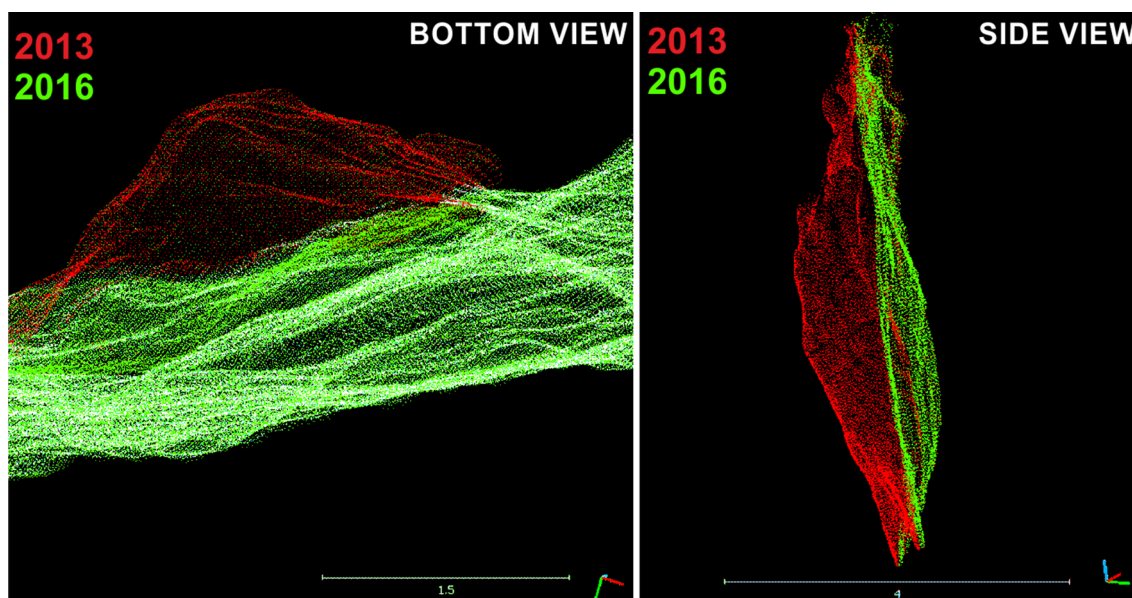

Fig. 5 Example of a unified 3D point cloud representing a collapsed rock block. The scale bar is in meters
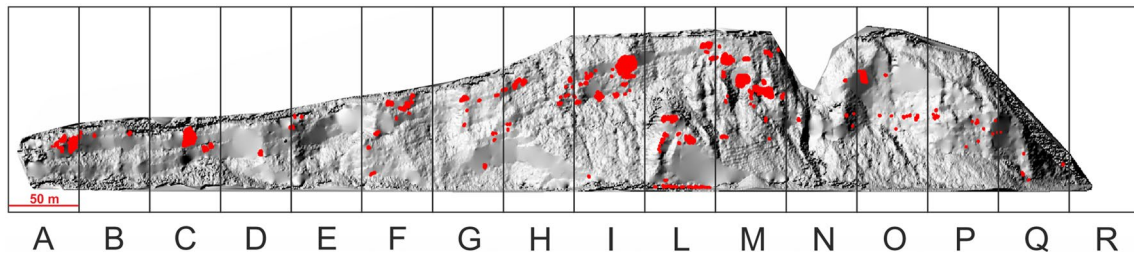
Fig. 6 Inventory of detected failures. Rectangles and letters identify the cliff sectors

were derived from the figures obtained with the previously described point-based procedure; the potentially unstable volume was calculated by multiplying the 3D-area of the sector for the maximum failure thickness estimated along the analyzed cliff, equal to 2.8 m. The assumption of multiplying by 2.8 m, rather than by the maximum sector-related failure thickness, was taken to make the statistical analysis homogeneous.

At this stage, to provide an overall characterization of recession that affected the 16 cliff sectors in the considered time span, the following indexes were computed, together with the average retreat rates. The area and the volume ratio indexes were expressed as percentage and computed as follows:

$$\text{Area ratio index} = \frac{\text{Sum of the 2D scar areas of the sector}}{\text{2D area of the sector}},$$

$$\text{Volume ratio index} = \frac{\text{Sum of the volumes lost in the sector}}{\text{(Unstable) Volume of the sector}}.$$

The average cliff retreat rates were calculated for sectors that experienced significant collapses in terms of displaced volumes ($> 10\ \text{m}^3$), by using a modified version of the formula proposed by Young and Ashford (2006):

$$R = \frac{\text{Volume of rocks collapsed in the sector}}{\text{(3D area of the sector)} \times 3},$$

where R is the retreat rate expressed in m/year, and 3 is the approximate number of years considered in this study.

The amount of detached blocks occurred in each geological formation was calculated by overlapping the two datasets in ArcGis, on the *YZ* projection plane.

4 Results

4.1 Change detection results and statistical data

The co-registration errors calculated for each couple of compared point clouds are summarized in Table 1. Errors obtained with the empirical approach and used for the M3C2 analyses (fifth column in Table 1) are comparable with those estimated automatically by the RealWorks software after the alignment procedure (sixth column). This confirms the suitability of the used empirical procedure, and the negligible impact of the occurred failures on the ICP alignment results.

The change detection analysis allowed identifying a total of 191 cliff failures (Fig. 6). Among them, 32 failures were identified also with the visual inspection of two sets of photos taken during the 2013 and 2016 field surveys. One example is represented in Fig. 7 where, among the significant changes, both a collapsed rock block of 11 m³ and vegetation changes are highlighted. In this case, vegetation was not removed intentionally to evidence both accuracy of the used technique and the importance of vegetation filtering before performing change detection analyses like this. Moreover, it is worth noting that redundant changes, due to the partial

Table 1 Results of the empirical error analysis corresponding to each pair of compared point clouds

Compared point clouds	Number of patches	Mean distances, μ (m)	Mean standard deviation, σ (m)	Error threshold, $\mu + 2\sigma$ (m)	Alignment error in RealWorks (m)
$C_{1,\,2013}$–$C_{1,\,2016}$	7	0.011	0.005	0.021	0.027
$C_{2,\,2013}$–$C_{2,\,2016}$	8	0.022	0.009	0.039	0.040
$C_{3,\,2013}$–$C_{3,\,2016}$	8	0.021	0.009	0.039	0.033
$C_{4,\,2013}$–$C_{4,\,2016}$	7	0.032	0.012	0.056	0.030
$C_{5,\,2013}$–$C_{5,\,2016}$	7	0.027	0.012	0.052	0.032

The fifth column shows the co-registration errors used for the change detection analysis. The sixth column shows the ICP alignment errors calculated by RealWorks software
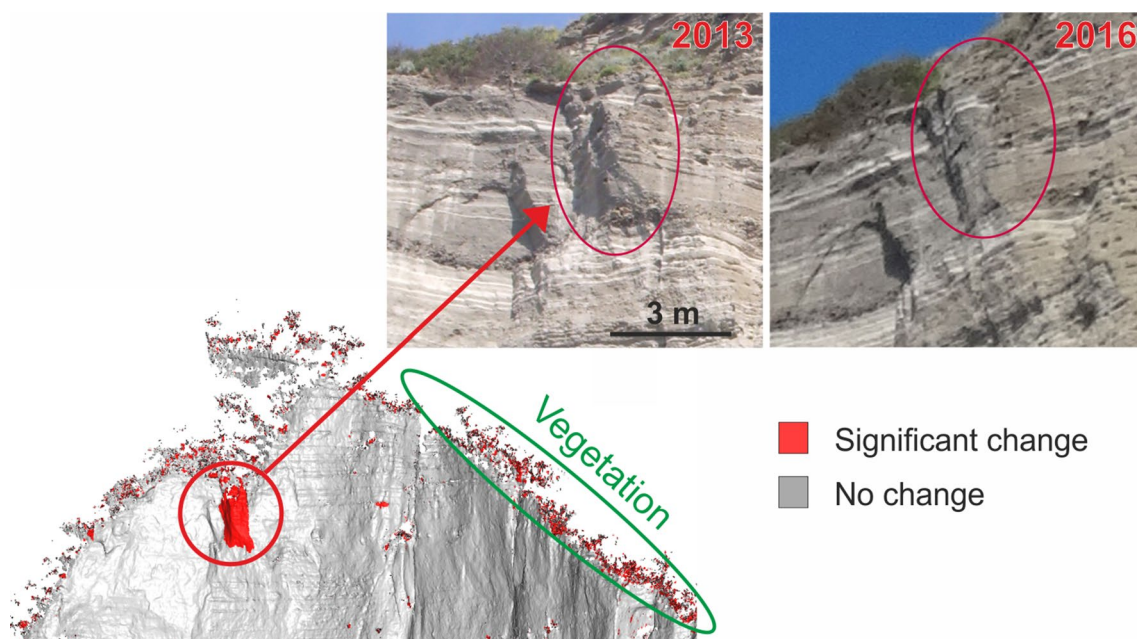
Fig. 7 Example of a collapsed rock block and related photographic comparison

Table 2 Amount of detached rock blocks detected in each cliff-forming geological formation

Geological formation	Amount of detached blocks (%)
Neapolitan Yellow Tuff	28
Solchiaro	10
Campanian Ignimbrite	0.1
Serra	33.5
Vivara	28.4

overlapping of point clouds acquired during the same survey, were manually selected and discarded.

The detached rock blocks resulted distributed along the entire Torrefumo cliff face with an apparent concentration toward the cliff edge, and in correspondence of the steepest and erodible slopes. The results of the overlap between the blocks and geological formations are shown in Table 2. It is quite evident that most of the detected failures are concentrated in the Serra, Solchiaro and Neapolitan Yellow Tuff formations (71.6%) with respect to the ones affecting the Vivara oldest unit (28.4%).

The detached blocks ranged between 0.01 and 1 m as mean thickness, 0.001 and 150 m^3 in volume, while 2D scar areas varied between 0.1 and 330 m^2. The absolute frequency distribution of volumes was organized into 6 logarithmic bins. Failures between 0.01 and 1 m^3 revealed to be the most frequent, whereas only one block resulted larger than 100 m^3. The two magnitude-frequency distributions shown in Fig. 8, and expressed in terms of displaced volume in a log–log chart, follow inverse power laws, with exponents of 0.479 and 0.6. The curve with exponent 0.479 approximates the volumes of all the detected failures, whereas the curve with exponent 0.6 refers to volumes larger than 0.03 m^3. By comparing the two different R^2, volumes greater than 0.03 m^3 are those well fitted by power law, with R^2 of 0.981, highlighting a possible rollover effect due to the limited amount of small-scale failures (< 0.03 m^3). In general, the order of magnitude of the two exponents is quite lower with respect to those of power laws describing volumetric data in other cliff settings (e.g., Gilham et al. 2018; Williams et al. 2018; Marques 2008). The 90th percentile of the entire volumetric distribution is equal to 2.35 m^3.

Both scatters correlating the mean thickness with the scar area, and the scar area with the volume were also examined. The mean thickness-area data are characterized by high scatter (Fig. 9), indicating a considerable heterogeneity of blocks geometry, whereas the volume increases proportionally with the growth of the scar area, following a positive power law trend as shown by the exponent of 1.4 (Fig. 10). However, dots remain below the dashed line representing a mean failure thickness of 1 m, and the scatter around the central tendency line is limited, highlighting a homogenous volume-area growth. Similar area-volume relationships related to coastal cliff failures were found by Caputo et al. (2018) for a tuffaceous cliff near the study area, Benjamin et al. (2016) in UK, as well as by other authors for different types of landslides in various geological settings worldwide (Guzzetti et al. 2009 and references therein).
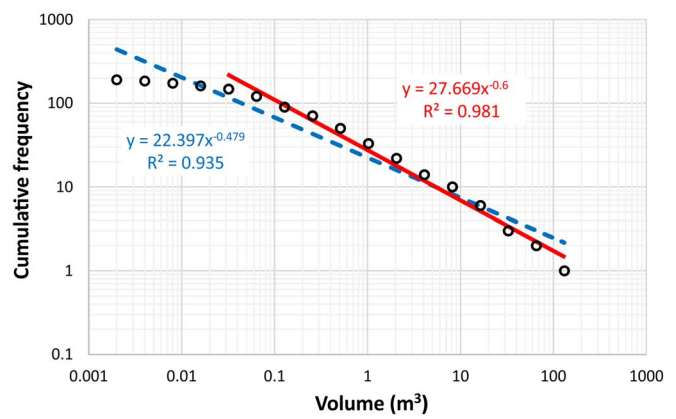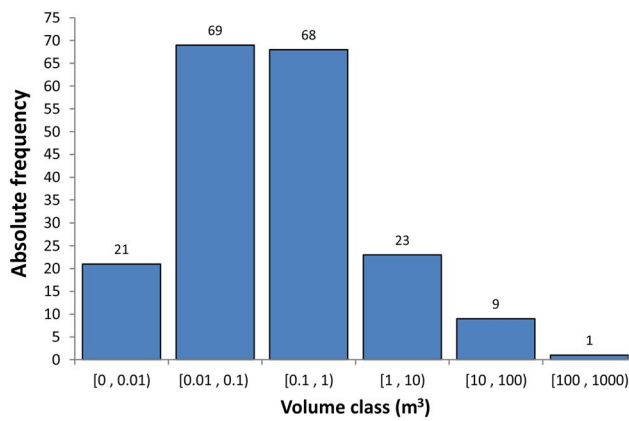
Rendiconti Lincei. Scienze Fisiche e Naturali (2020) 31:337–351

345

Fig. 8 On the left, histogram showing the absolute frequency of failure volumes obtained using logarithmic bins; the 90th percentile is equal to 2.35 m³. On the right, cumulative frequency distribution of failure volumes in a log–log chart; the dashed line represents the power law approximating all data, while the solid line is the power law related to volumes greater than 0.03 m³
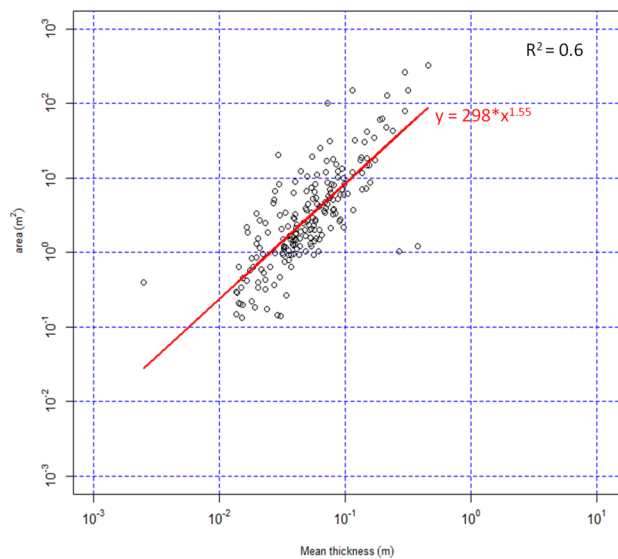

Fig. 9 Mean thickness versus scar area in a log–log scatter plot. The power law regression line is highlighted
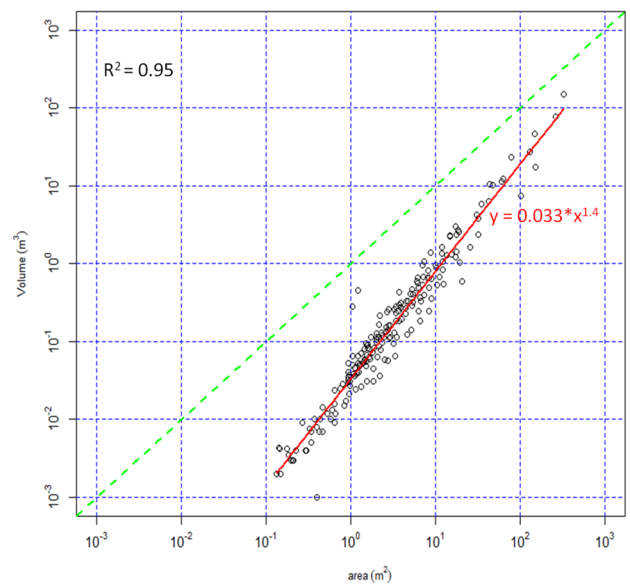

Fig. 10 Scar area versus volume in a log–log scatter plot. The power law regression line is highlighted; the dashed line represents a mean failure thickness equal to 1 m

Figure 11 shows statistics on the spatial distribution of detected failures, as well as on the area and volume ratios, with respect to the cliff sectors represented in Fig. 6. The most relevant findings can be summarized as follows: (i) sectors A and C have the highest area and volume ratios but a low frequency of detached blocks; (ii) sectors F, I and M have a significant area ratio and a high frequency of detached blocks but a moderate volume ratio; (iii) sector L has a very high frequency of detached blocks and a low area ratio, whereas the volume ratio is negligible. Statistics of the remaining sectors do not show particular behaviors.

The average retreat rates are reported in Table 3. These range from a minimum of 0.001 to 0.025 m/year and refer only to sectors displaying a significant volume loss; other sectors are characterized by negligible detached volumes with null consequent rates. The average retreat rate of the entire analyzed cliff segment is about 0.003 m/year. It is worth noting that this rate is based on only two epochs covering a time span of about three years, and refers to a specific interval of a broader cliff recession cycle. In addition, it is important to underline that long-term cliff retreat rates (greater than 10–100 years) may be lower than short-term (e.g., monthly or annual) rates, which are often influenced by large-magnitude and episodic erosion events. In the light of this, Williams et al. (2018) demonstrated that the analysis of cliff recession is a kind of trade-off in

Fig. 11 Statistics calculated for each cliff sector
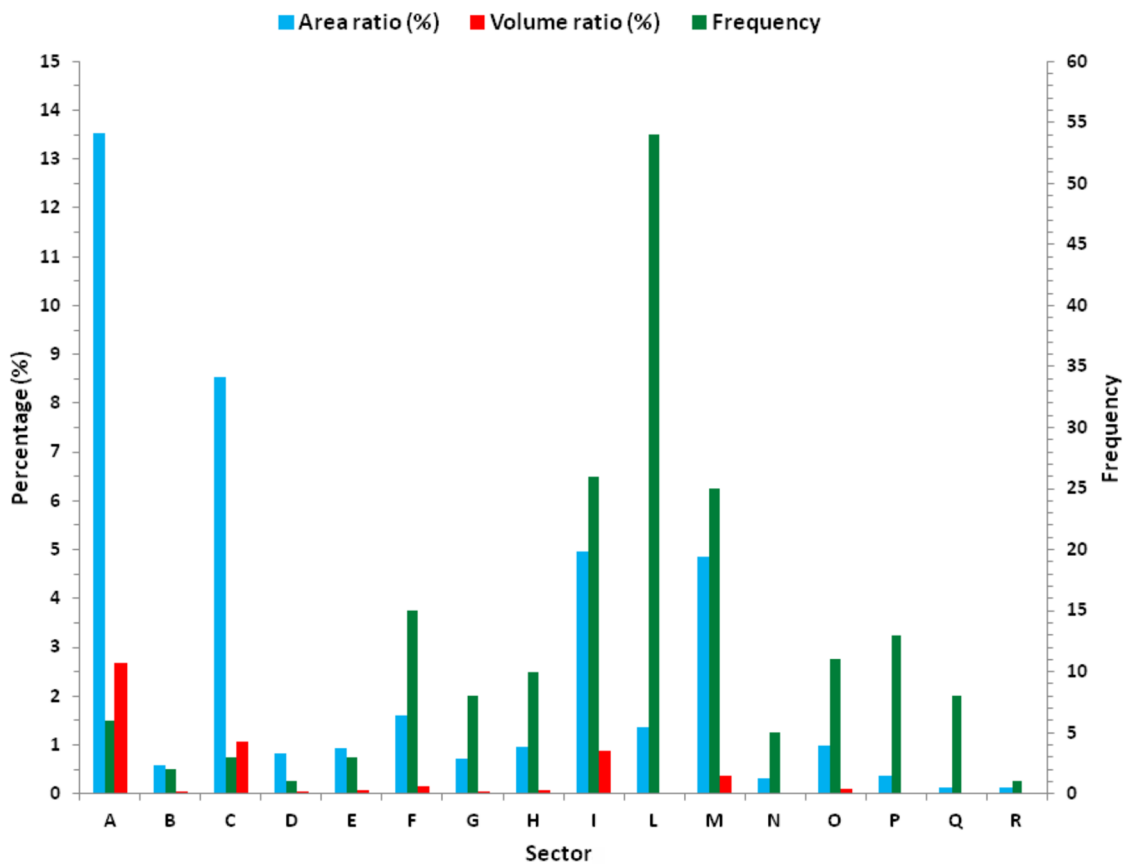
SECTOR DATA				FAILURES DATA			RATIO	
SECTOR	3D AREA (m²)	2D AREA (m²)	VOLUME (m³)	FREQUENCY	2D AREA (m²)	VOLUME (m³)	AREA (%)	VOLUME (%)
A	1156.5	739	3238.1	6	100	86.9	13.532	2.683
B	1927.2	1240.8	5396	2	7.4	2.8	0.593	0.051
C	2937.1	1332.9	8224	3	113.6	86.7	8.522	1.054
D	1802.4	864.2	5046.7	1	7.2	2.7	0.833	0.054
E	1882.8	996.6	5272	3	9.3	3.8	0.934	0.072
F	3167.2	2300	8868.2	15	37	13.2	1.608	0.149
G	3754.8	2651.9	10513.3	8	19.3	5.1	0.729	0.048
H	5360	3426.7	15008.1	10	32.6	10.2	0.952	0.068
I	6759.4	3948.9	18926.4	26	196.2	166.7	4.969	0.881
L	5902.4	3624.1	16526.8	54	49.3	4.7	1.361	0.028
M	7176.1	4434.2	20093	25	214.7	75.5	4.842	0.376
N	7118.8	3413.1	19932.7	5	10.9	2.9	0.320	0.014
O	4597.6	3239.3	12873.4	11	31.7	12.4	0.979	0.096
P	4309.4	2856.8	12066.3	13	10.3	1.6	0.362	0.014
Q	2002.9	1491.7	5608.2	8	1.8	0.3	0.119	0.005
R	616.3	433.6	1725.8	1	0.5	0.1	0.115	0.003
TOTAL	60471	36993.8	169318.9	191	841.8	475.3		

Table 3 Average annual retreat rate of cliff sectors characterized by a volume loss greater than 10 m³

Sector	A	C	F	H	I	M	O
R_{sector} (m/year)	0.025	0.010	0.001	0.001	0.008	0.004	0.001

spatial and temporal resolution of monitoring, underlining the relevant potential of high-frequency measurements for the accurate evaluation of magnitude–frequency derivatives, such as hazard return intervals and erosion rates.

4.2 Field evidences of different cliff retreat mechanisms

The cross section of Fig. 12 was drawn based on a point cloud acquired during the 2016 TLS survey. The profile intersects a succession of tuff layers and ash deposits

Rendiconti Lincei. Scienze Fisiche e Naturali (2020) 31:337–351

347

characterized by variable thicknesses and compactness. A series of convexities and concavities are localized respectively in correspondence of the welded tuff and loose ash layers, indicating an evident topographic signature of the different response to erosion (i.e. selective erosion). Locally within the cliff, in correspondence of such lithological variations, scars related to rock falls have been recognized (Fig. 13).

In addition to ash-tuff successions, poorly welded pumices outcrop locally within the Torrefumo cliff. In correspondence of these deposits, a relatively slow and diffused (i.e. "grain-by-grain") erosional process (e.g., Dong and Guzzetti 2005) has been detected during the TLS surveys. Figure 13 shows, for example, excavation-shape morphologies ostensibly produced by this mechanism, which are linked at the cliff toe to a debris cone likely formed by pumices eroded from the overlying deposits. The described change detection procedure allowed quantifying the volume gained to the cone between the two TLS surveys in about 25 m^3.
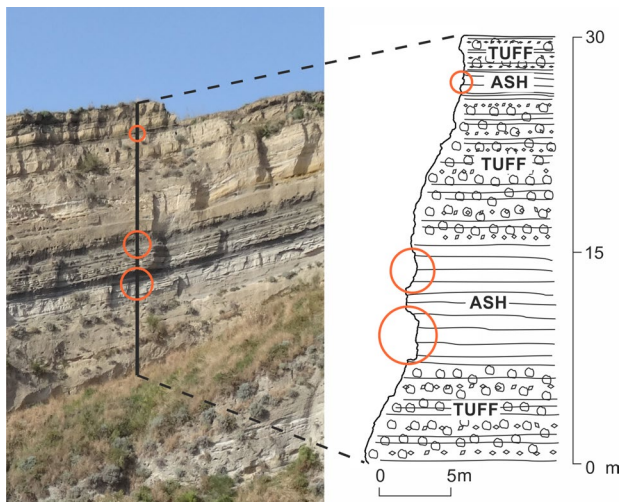
5 Discussion

The results of our analysis suggest that, despite the protective action of the seawall at the cliff toe, the retreat of the Torrefumo cliff is still active and it occurs by means of different mechanisms of slope instability. The used techniques allowed identifying 191 failures that resulted distributed along the entire analyzed cliff face (Fig. 6). An overall interpretation of histograms in Fig. 11 suggests that the western and central sectors (from A to M) experienced the most significant instability processes in terms of involved areas, volumes and frequency of failures. Conversely, the eastern sectors of the cliff (from N to R) resulted more stable. This trend was also confirmed by different retreat rates (Table 3) and was ostensibly controlled by geological factors, as the presence of more resistant rocks in the eastern cliff side (e.g., well-welded tuff included within the Vivara Formation), compared to the weakly welded layers of pumice and ash, very prone to instability processes, outcropping in the
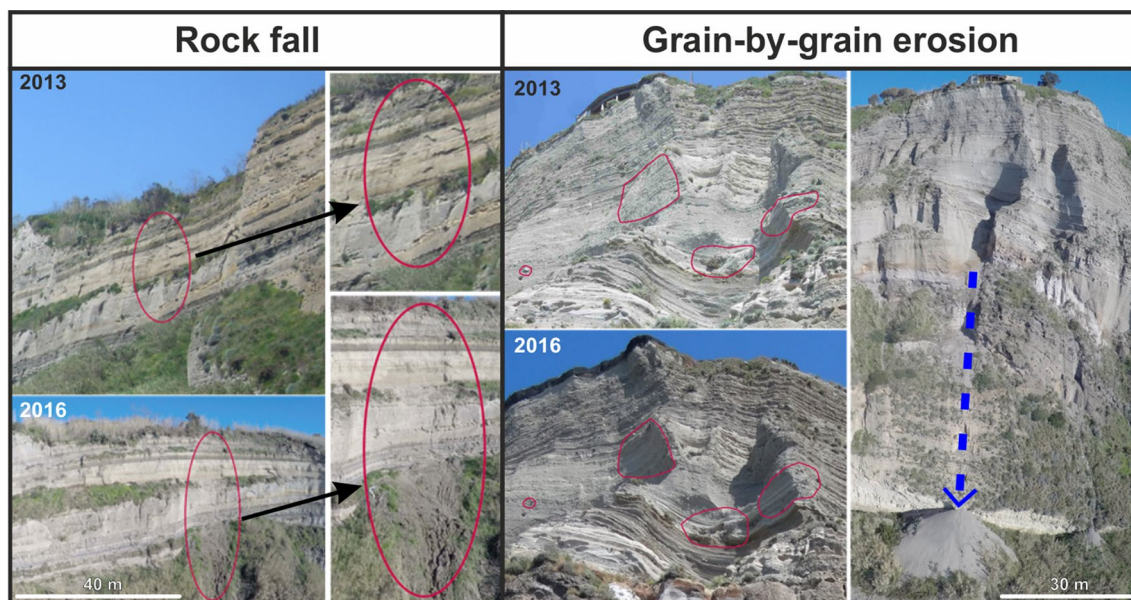

Fig. 12 High-resolution cross-section highlighting topographic variations in correspondence of the outcropping lithological units. Specifically, concavities (circles) are in correspondence of fine-ash layers whereas convexities are in correspondence of tuffaceous layers

Fig. 13 Multitemporal images of cliff portions affected by different types of failures

western side (e.g., deposits belonging to the Serra and Solchiaro Formations). This was also highlighted by the data shown in Table 2.

Among statistics represented in Fig. 11, the area and volume ratio indexes indicate that sectors A and C were affected by a limited number of failures (i.e. 6 and 3, respectively) that however displaced significant rock volumes, namely of 86.9 m^3 and 86.7 m^3. These data indicate that, in these sectors, episodic high-magnitude cliff failures induced sudden and localized cliff recessions, as also highlighted by relatively high retreat rates of 0.025 and 0.010 m/years (Table 3).

Sectors F, I and M are characterized instead by relevant area ratio indexes and frequency of block failures, but moderate volume ratios. This can be explained by the occurrence of frequent small-scale failures (between 10^{-2} and 1 m^3), probably affecting incoherent deposits of ash, pumice and scoria. A similar behavior results for the sector L, even though the negligible volume ratio index, in this case, indicates that failures were more superficial. In this sector, in fact, tuffaceous units are characterized by enlarging tafoni that are degrading the rock surface. The occurrence of tafoni supports the hypothesis that wind action and salt weathering may cause their progressive enlargement by means of the spalling of small-scale rock fragments (Doehne 2002).

The frequency-volume distributions shown in Fig. 8 follow inverse power laws, as resulted for many cliff sites throughout the world. Similar distributions, for instance, were found by Rosser et al. (2005), Lim et al. (2010) and Dewez et al. (2013). Most of the detached rock volumes are smaller than 1 m^3, whereas the largest one is ca. 150 m^3. It is worth noting that rock volumes < 0.03 m^3 are scarcely fitted by the general power law, as highlighted by an $R^2 = 0.935$. This value is, in fact, lower than $R^2 = 0.981$ associated with the power law fitting volumes larger than 0.03 m^3. This indicates a possible rollover effect, as recognized in many landslide frequency-magnitude distributions (Tebbens 2020 and references therein). A similar behavior was also found by Van Veen et al. (2017) in analyzing a rock fall dataset with different sampling intervals (duration between scans). Generally, the rollover effect is the result of the undersampling of smaller failures and therefore to the inventory resolution (Stark and Hovius 2001; Guzzetti et al. 2002). In this study, given the relevant accuracy of the TLS-based method that allowed detecting failures up to 10^{-3} m^3, no censoring effects seem to cause it. A possible reason may be the coalescence of multiple small scars to form larger failures, that is more likely in the case of excessively long time intervals between the acquired scans (Barlow et al. 2012; Tonini and Abellán 2014; Carrea et al. 2015; van Veen et al. 2017). Williams et al. (2018), for example, noted that while a rollover occurred applying a frequency of TLS surveys of 30 days, this was not apparent at a frequency lower than

1 h, suggesting that the observed rollover occurred due to superimposition and coalescence of small-scale events as consequence of longer return periods between surveys. In such cases, small-scale failures that could not be mapped at their correct size bins are transferred into larger bins, causing a divergence from the power law (Tanyaş et al. 2019). In fact, as highlighted by Tebbens (2020), the lower the scaling exponent (or less steep the power function) is, the greater the contribution of large events relative to small events will be. In the light of this, and besides the probable coalescence conditions, larger displacements like those represented in Fig. 13 and described in the Sect. 4.2 were effectively documented, contributing to reduce the slope of power laws and hence the scaling exponents.

The estimated volume range of failures was also controlled by the geological setting of the cliff. The different types of volcaniclastic deposits in fact respond in different ways to surface erosion processes (Fig. 12), and our findings indicate that the grain-by-grain mechanism affects the most erodible deposits, mobilizing limited amounts of material, which is also suggested by the grown of the debris cone in Fig. 13, evaluated in 25 m^3 in about three years. Locally, instead, erosion may trigger high-magnitude failures (Figs. 7, 13) that occur as rock fall or slide and displace large blocks also larger than a hundred of cubic meters, even if with a limited thickness. These outcomes are in accordance with the area/volume relationship (Fig. 10), indicating, in fact, a general superficial character of all the detected failures that show a mean thickness lower than 1 m. The relatively shallow behavior of these failures could be related to the surface erosion involving the most erodible deposits (Fig. 13), as well as to the collapses of the most degraded rock outcrops, or unstable blocks isolated by selective erosion (Figs. 7, 13).

Investigation of the structural control on the Torrefumo cliff failures was out of the aims of this study. However, field evidences and the results presented in the previous paragraphs suggest that the structural pattern has a negligible effect on the instability processes of the Torrefumo cliff, compared to geotechnical properties of rocks. This is in accordance with the findings reported by Bird (2008), who stated that coastal cliff profiles and retreat rates are mostly controlled by rock resistance and exposure to weathering and erosion.

It is important to highlight two factors that limit the effectiveness of multitemporal TLS in the analysis of sea cliffs. The main constrain consists of the temporal scale of measurements. According to Earlie (2015), measurements performed at time intervals in the order of a few years provide only an indication of the occurred changes but do not include adequate spatial and temporal resolution that are necessary for a detailed analysis. In fact, only more frequent measurements may be effective in: (i) discriminating

between continuous and sporadic changes; (ii) relate forcing mechanisms to failure, as coastal cliffs may experience massive changes during storm events or respond to other drivers with a seasonal behavior. On the other hand, it is commonly difficult to identify an adequate or ideal survey frequency or duration that may provide a complete reconstruction of rates and patterns of coastal cliff erosion (Rosser et al. 2017). In the case of the Torrefumo cliff, Esposito et al. (2018) had quantified mean annual retreat rates of 1.2 m/year and 0.17 m/year for the periods 1956–1974 and 1974–2008, respectively. These values are quite different from the average rate of 0.003 m/year (2013–2016) estimated in the present work, ostensibly because of the different temporal scales and of the geomorphic conditions that changed through time. We infer that the retreat rates we obtained for the different cliff sectors may be related to a specific interval of a broad cliff recession cycle that requires more measurements to be fully addressed. Nevertheless, the average retreat rate is definitely comparable with rates documented for similar time intervals, and various geological settings, by Wangensteen et al. (2007) in Svalbard, Marques (2006) in Portugal, Greenwood and Orford (2007) in Ireland.

Further measurements to be carried out in the study area, using innovative techniques like the structure-from-motion photogrammetry based on UAV and other mobile platforms (Esposito et al. 2017a; Dewez et al. 2016), may be helpful to overcome the lack of data from some portion of the cliff that could not be scanned so far (e.g., Fig. 3) because of scanner positioning issues.

6 Conclusions

In this study, repeated TLS surveys were performed in the years 2013 and 2016 along the Torrefumo coastal cliff, without the use of targets and GCPs. An ICP algorithm was used to align multitemporal 3D point clouds in pairs, achieving a centimetric accuracy. Comparison of 2013 and 2016 point clouds allowed for the acquisition of a cliff failures inventory consisting of 191 events. Statistical analysis showed that: (1) the magnitude-frequency distribution of detected failures followed an inverse power law; (2) failure events larger than 100 m^3 occurred rarely in the considered time span; (3) events between 0.01 and 1 m^3 were the most frequent, and the 90th percentile was equal to 2.35 m^3; (4) the types of instability processes varied over the cliff face and consisted mainly in rock falls and grain-by-grain erosion. Both field survey and analysis of the 3D point clouds showed that a selective erosion is effectively contributing to the cliff retreat, creating conditions for the triggering of block failures.

The TLS approach adopted in this work proved to be an accurate method to develop a catalogue of cliff failures.

Resolution and accuracy of data allowed for a full range of failures to be recognized and measured. This improved the frequency-volume analysis, providing preliminary data for quantitative risk assessments. The detected failures confirmed that the cliff is still retreating, although the action of the seawall is limiting the sea wave erosion. In the future, TLS monitoring of the Torrefumo coastal cliff at higher temporal resolution may provide a valid support to local authorities for the coastal zone management, and planning of suitable countermeasures aimed at reducing risk conditions affecting several buildings realized close to the retreating cliff edge.

Compliance with ethical standards

Conflict of interest The authors declare that they have no conflict of interest.

Authorship disclosure All the listed authors have approved the manuscript before submission.

Participant disclosure The research did not involve human participants and animals.

References

Barlow J, Lim M, Rosser N, Petley D, Brain M, Norman E, Geer M (2012) Modeling cliff erosion using negative power law scaling of rockfalls. Geomorphology 139–140:416–424

Barnhart TB, Crosby BT (2013) Comparing two methods of surface change detection on an evolving thermokarst using high-temporal frequency terrestrial laser scanning, Selawik River, Alaska. Remote Sens 5(6):2813–2837

Benjamin J, Rosser NJ, Brain MJ (2016) Rockfall detection and volumetric characterisation using LiDAR. In: Aversa S, Cascini L, Picarelli L, Scavia C (eds) Landslides and engineered slopes, experience, theory and practice: proceedings of the 12th international symposium on landslides, Napoli, Italy, 12–19 June 2016. CRC Press, Delft, pp 389–395

Besl P, McKay H (1992) A method for registration of 3-D shapes. IEEE Trans Pattern Anal Mach Intell 14(2):239–256

Bird E (2008) coastal geomorphology: an introduction, 2nd edn. Wiley, England

Brunetti MT, Guzzetti F, Rossi M (2009) Probability distributions of landslide volumes. Nonlinear Process Geophys 16:179–188

Caputo T, Marino E, Matano F, Somma R, Troise C, De Natale G (2018) Terrestrial laser scanning (TLS) data for the analysis of

coastal tuff cliff retreat: application to Coroglio cliff, Naples Italy. Ann Geophys. https://doi.org/10.4401/ag-7494

Carrea D, Abellán A, Derron M-H, Jaboyedoff M (2015) Automatic rockfall volume estimation based on terrestrial laser scanning data. Eng Geol Soc Territ 2:425–428

Collins BD, Sitar N (2008) Processes of coastal bluff erosion in weakly lithified sands, Pacifica, California, USA. Geomorphology 97(3):483–501

Collins B, Corbett S, Fairly H, Minasian D, Kayen R, Dealy T, Bedford D (2012) Topographic change detection at select archeological sites in Grand Canyon National Park, Arizona, 2007–2010. US Geologic Survey Scientific Investigation Report 2012-5133, US Geological Survey, Reston, Virginia, p 77

Darmawan H, Walter TR, Brotopuspito KS, Subandriyo Nandaka IGMA (2018) Morphological and structural changes at the Merapi lava dome monitored in 2012–15 using unmanned aerial vehicles (UAVs). J Volcanol Geotherm Res 349:256–267

Dewez TJB, Rohmer J, Regard V, Cnudde C (2013) Probabilistic coastal cliff collapse hazard from repeated terrestrial laser surveys: case study from Mesnil Val (Normandy, northern France). J Coast Res 65:702–707

Dewez T, Leroux J, Morelli S (2016) Cliff collapse hazard from repeated multicopter uav acquisitions: return on experience. Int Arch Photogramm XLI-B5:805–811

Doehne E (2002) Salt weathering: a selective review. In: Siegesmund S, Weiss T, Vollbrecht A (eds) Natural stone, weathering phenomena, conservation strategies and case studies. Geological Society, London, pp 51–64

Dong P, Guzzetti F (2005) Frequency-size statistics of coastal soft-cliff erosion. J Waterw Port Coast Ocean Eng 131(1):37–42

Earlie CS (2015) Field observations of wave induced coastal cliff erosion, Cornwall, UK. PhD Dissertation, Plymouth University

Esposito G, Salvini R, Matano F, Sacchi M, Danzi M, Somma R, Troise C (2017a) Multitemporal monitoring of a coastal landslide through SfM-derived point cloud comparison. Photogramm Rec 32(160):459–479

Esposito G, Mastrorocco G, Salvini R, Oliveti M, Starita P (2017b) Application of UAV photogrammetry for the multi-temporal estimation of surface extent and volumetric excavation in the Sa Pigada Bianca open-pit mine, Sardinia, Italy. Environ Earth Sci 76:103

Esposito G, Salvini R, Matano F, Sacchi M, Troise C (2018) Evaluation of geomorphic changes and retreat rates of a coastal pyroclastic cliff in the Campi Flegrei volcanic district, southern Italy. J Coast Conserv. https://doi.org/10.1007/s11852-018-0621-1

Fey C, Wichmann V (2017) Long-range terrestrial laser scanning for geomorphological change detection in alpine terrain–handling uncertainties. Earth Surf Process Landf 4:789–802

Gilham J, Barlow J, Moore R (2018) Marine control over negative power law scaling of mass wasting events in chalk sea cliffs with implications for future recession under the UKCP09 medium emission scenario. Earth Surf Process Landf 43(10):2136–2146

Greenwood RO, Orford JD (2007) Factors controlling the retreat of Drumlin coastal cliffs in a low energy marine environment–Strangford Lough, Northern Ireland. J Coast Res 23:285–297

Guzzetti F, Malamud B, Turcotte D, Reichenbach P (2002) Power-law correlations of landslide areas in central Italy. Earth Plan Sci Lett 195:169–183

Guzzetti F, Ardizzone F, Cardinali M, Rossi M, Valigi D (2009) Landslide volumes and landslide mobilization rates in Umbria, central Italy. Earth Planet Sci Lett 279(3–4):222–229

Hungr O, Evans S, Hazzard J (1999) Magnitude and frequency of rock falls and rock slides along the main transportation corridors of southwestern British Columbia. Can Geotech J 36:224–238

Katz O, Mushkin A (2013) Characteristics of sea-cliff erosion induced by a strong winter storm in the eastern Mediterranean. Quat Res 80(1):20–32

Kazhdan M, Botitho M, Hoppe H (2006) Poisson surface reconstruction. In: Proceedings of the fourth eurographics symposium on geometry processing, pp 61–70

Kromer RA, Hutchinson DJ, Lato MJ, Gauthier D, Edwards T (2015) Identifying rock slope failure precursors using LiDAR for transportation corridor hazard management. Eng Geol 195:93–103

Kromer R, Abellán A, Hutchinson J, Lato M, Jaboyedoff M (2017) Automated terrestrial laser scanning with near real-time change detection—monitoring of the séchilienne landslide. Earth Surf Dyn 5:293–310

Kuhn D, Prüfer S (2014) Coastal cliff monitoring and analysis of mass wasting processes with the application of terrestrial laser scanning: a case study of Rügen, Germany. Geomorphology 213:153–165

Lague D, Brodu N, Leroux J (2013) Accurate 3D comparison of complex topography with terrestrial laser scanner: application to the Rangitikei canyon (N-Z). ISPRS J Photo Remote Sens 82:10–26

Letortu P, Costa S, Maquaire O, Delacourt C, Augereau E, Davidson R, Suanez S, Nabucet J (2015) Retreat rates, modalities and agents responsible for erosion along the coastal chalk cliffs of Upper Normandy: the contribution of terrestrial laser scanning. Geomorphology 245:3–14

Lim M, Rosser NJ, Allison RJ, Petley DN (2010) Erosional processes in the hard rock coastal cliffs at Staithes, North Yorkshire. Geomorphology 114(1–2):12–21

Lim M, Rosser NJ, Petley DN, Keen M (2011) Quantifying the controls and influence of tide and wave impacts on coastal rock cliff erosion. J Coast Res 27:46–56

Malamud BD, Turcotte D, Guzzetti F, Reichenbach P (2004) Landslide inventories and their statistical properties. Earth Surf Process Landf 29:687–711

Marques F (2006) A simple method for the measurement of cliff retreat from aerial photographs. Zeit f Geomorph 144:39–59

Marques F (2008) Magnitude-frequency of sea cliff instabilities. Nat Hazards Earth Syst Sci 8:1161–1171

Martino S, Mazzanti P (2014) Integrating geomechanical surveys and remote sensing for sea cliff slope stability analysis: the Mt. Pucci case study (Italy). Nat Hazards Earth Syst Sci 14:831–848

Matano F, Pignalosa A, Marino E, Esposito G, Caputo T, Somma R, Sacchi M, Troise C, De Natale G (2015) Laser scanning application for geostructural analysis of tuffaceous coastal cliffs: the case of Punta Epitaffio, Pozzuoli Bay, Italy. Eur J Remote sens 48:615–637

Matano F, Iuliano S, Somma R, Marino E, Del Vecchio U, Esposito G, Molisso F, Scepi G, Grimaldi GM, Pignalosa A, Caputo T, Troise C, De Natale G, Sacchi M (2016) Geostructure of Coroglio tuff cliff, Naples (Italy) derived from terrestrial laser scanner data. J Maps 12(3):407–421

Orsi G, De Vita S, Di Vito M (1996) The restless resurgent Campi Flegrei nested caldera (Italy): constraints on its evolution and configuration. J Volcanol Geotherm Res 74:179–214

Passalacqua P, Belmont P, Staley DM, Simley JD, Arrowsmith JR, Bode CA, Crosby C, Delong SB, Glenn NF, Kelly SA, Lague D, Sangireddy H, Schaffrath K, Tarboton DG, Wasklewicz T, Wheaton JM (2015) Analyzing high resolution topography for advancing the understanding of mass and energy transfer through landscapes: a review. Earth Sci Rev 148:174–193

Pelletier J, Malamud B, Blodgett T, Turcotte D (1997) Scale-invariance of soil moisturevariability and its implications for the frequency-size distributions of landslides. Eng Geol 48:255–268

Perrotta A, Scarpati C, Luongo G, Morra V (2006) The Campi Flegrei caldera boundary in the city of Naples. In: De Vivo B (ed)

Volcanism in the campania plain: vesuvius, campi flegrei and ignimbrites. Elsevier, Amsterdam, pp 85–96

Perrotta A, Scarpati C, Luongo G, Morra V (2011) Stratigraphy and volcanological evolution of the southwestern sector of Campi Flegrei and Procida Island, Italy. Geol Soc Am Spec Pap 464:171–191

Rohmer J, Dewez T (2015) Analysing the spatial patterns of erosion scars using point process theory at the coastal chalk cliff of Mesnil-Val, Normandy, northern France. Nat Hazards Earth Syst Sci 15:349–362

Rosi M, Sbrana A (1987) The Phlegrean fields. Consiglio Nazionale delle Ricerche, Quaderni de "La Ricerca Scientifica, Rome

Rosi M, Vezzoli L, Aleotti P, De Censi M (1996) Interaction between Caldera collapse and eruptive dynamics during the Campanian Ignimbrite eruption, Phlegrean fields, Italy. Bull Volcanol 57:541–554

Rosser NJ, Petley DN, Lim M, Dunning SA, Allison RJ (2005) Terrestrial laser scanning for monitoring the process of hard rock coastal cliff erosion. Q J Eng Geol Hydrogeol 38:363–375

Rosser NJ, Lim M, Petley DN, Dunning SA, Allison RJ (2007) Patterns of precursory rockfall prior to slope failure. J Geophys Res 112:F04014

Rosser N, Williams J, Hardy R, Brain M (2017) Insights from high frequency monitoring of coastal cliff erosion. Geophysical Research Abstracts 19, EGU2017-4749-1

Santana D, Corominas J, Mavrouli O, Garcia-Sellés D (2012) Magnitude–frequency relation for rockfall scars using a terrestrial laser scanner. Eng Geol 145–146:50–64

Scarpati C, Cole P, Perrotta A (1993) The Neapolitan Yellow Tuff—a large volume multiphase eruption from Campi Flegrei, southern Italy. Bull Volcanol 55:343–356

Somma R, Matano F, Marino E, Caputo T, Esposito G, Caccavale M, Carlino S, Iuliano S, Mazzola S, Molisso F, Sacchi M, Troise G, De Natale G (2015) Application of laser scanning for monitoring coastal cliff instability in the Pozzuoli Bay, Coroglio Site, Posillipo Hill, Naples. Eng Geol Soc Terrt 5:687–690

Stark CP, Guzzetti F (2009) Landslide rupture and probability distribution of mobilized debris volumes. J Geophys Res 114:F00A02

Stark CP, Hovius N (2001) The characterization of landslide size distribution. Geophys Res Lett 28:1091–1094

Tanyaş H, van Westen CJ, Allstadt KE, Jibson RW (2019) Factors controlling landslide frequency—area distributions. Earth Surf Process Landf 44:900–917

Tebbens SF (2020) Landslide scaling: a review. Earth Space Sci 7:e2019EA000662

Tonini M, Abellán A (2014) Rockfall detection from LiDAR point clouds: a clustering approach using R. J Spat Inf Sci 8:95–110

van Veen M, Hutchinson DJ, Kromer R, Lato M, Edwards T (2017) Effects of sampling interval on the frequency-magnitude relationship of rockfalls detected from terrestrial laser scanning using semi-automated methods. Landslides 14:1579–1592

Wangensteen B, Eiken T, Ødegård RS, Sollid JL (2007) Measuring coastal cliff retreat in the Kongsfjorden area, Svalbard, using terrestrial photogrammetry. Polar Res 26:14–21

Westoby MJ, Dunning SA, Woodward J, Hein AS, Marrero SM, Winter K, Sugden DE (2016) Interannual surface evolution of an Antarctic blue-ice moraine using multi-temporal DEMs. Earth Surf Dyn 4:515–529

Williams JG, Rosser NJ, Hardy RJ, Brian MJ, Afana AA (2018) Optimising 4-D surface change detection: an approach for capturing rockfall magnitude-frequency. Earth Surf Dyn 6:101–119

Young AP, Ashford SA (2006) Application of airborne LIDAR for seacliff volumetric change and beach-sediment budget contributions. J Coast Res 22:307–318

Young AP, Guza RT, O'Reilly WC, Flick RE, Gutierrez R (2011) Short-term retreat statistics of a slowly eroding coastal cliff. Nat Hazards Earth Syst Sci 11:205–217